The growth of H II regions around massive stars: the role of metallicity and dust

Ahmad A. Ali ⓘ★

Department of Physics and Astronomy, University of Exeter, Stocker Road, Exeter EX4 4QL, UK

ABSTRACT

Gas metallicity (Z) and the related dust-to-gas ratio (f_d) can influence the growth of H II regions via metal line cooling and ultraviolet (UV) absorption. We model these effects in star-forming regions containing massive stars. We compute stellar feedback from photoionization and radiation pressure (RP) using Monte Carlo radiative transfer coupled with hydrodynamics, including stellar and diffuse radiation fields. We follow a $10^5\,M_\odot$ turbulent cloud with $Z/Z_\odot = 2$, 1, 0.5, and 0.1, and $f_d = 0.01\,Z/Z_\odot$ with a cluster-sink particle method for star formation. The models evolve for at least 1.5 Myr under feedback. Lower Z results in higher temperatures and therefore larger H II regions. For $Z \geq Z_\odot$, RP (P_{rad}) can dominate locally over the gas pressure (P_{gas}) in the inner half-parsec around sink particles. Globally, the ratio of P_{rad}/P_{gas} is around 1 ($2\,Z_\odot$), 0.3 ($Z_\odot$), 0.1 ($0.5\,Z_\odot$), and 0.03 ($0.1\,Z_\odot$). In the solar model, excluding RP results in an ionized volume several times smaller than the fiducial model with both mechanisms. Excluding RP and UV attenuation by dust results in a *larger* ionized volume than the fiducial case. That is, UV absorption hinders growth more than RP helps it. The radial expansion velocity of ionized gas reaches $+15\,\mathrm{km\,s^{-1}}$ outwards, while neutral gas has inward velocities for most of the runtime, except for $0.1\,Z_\odot$ that exceeds $+4\,\mathrm{km\,s^{-1}}$. Z and f_d do not significantly alter the star formation efficiency, rate, or cluster half-mass radius, with the exception of $0.1\,Z_\odot$ due to the earlier expulsion of neutral gas.

Key words: hydrodynamics – radiative transfer – stars: massive – ISM: clouds – H II regions.

1 INTRODUCTION

Stars form in clusters and associations inside giant molecular clouds (GMCs). In the Milky Way, the star formation efficiency (SFE; the proportion of gas mass converted into stars) is of the order of 10–30 per cent at the cluster scale and a few per cent at the global GMC scale (Lada & Lada 2003). This inefficiency may be explained by stellar feedback driven primarily by O stars (Matzner 2002). These massive stars are sources of energy and momentum for the interstellar medium via mechanisms such as photoionization, radiation pressure (RP), stellar winds, and supernovae (see e.g. the review by Dale 2015). In this paper, we focus on the radiative processes.

There remains much uncertainty as to the relative impact of the different feedback mechanisms. One way of assessing this is to compare the pressures associated with each process in a particular star-forming region. This has been done for a variety of H II regions in the Small and Large Magellanic Clouds (SMC and LMC, respectively; Lopez et al. 2011, 2014; Pellegrini, Baldwin & Ferland 2011; McLeod et al. 2019), in the Galactic Centre (Barnes et al. 2020), and more recently in the Galactic disc (Olivier et al. 2020). Most regions in these studies show low levels of RP compared to the thermal pressure from ionized gas, while other regions (typically the smaller ones) show the opposite result. This can also vary as a function of distance from the stellar sources, as in 30 Doradus in the LMC, where the inner region is dominated by RP and the outer parts by ionization.

One parameter that could modify the effectiveness of feedback is the metallicity, Z. The LMC and SMC have subsolar metallicities with $Z \approx 0.5$ and $0.2\,Z_\odot$, respectively (Russell & Dopita 1992). Observations show that metallicity varies within the Milky Way, decreasing with distance from the Galactic Centre where $Z \approx 2\,Z_\odot$ (Deharveng et al. 2000). This will factor into radiative transfer processes. The dominant cooling sources for ionized gas are collisionally excited forbidden lines from metal ions (Osterbrock & Ferland 2006). The dust-to-gas ratio is proportional to metallicity (Draine et al. 2007), and RP is exerted primarily on to dust grains that can be dynamically coupled to the gas. Furthermore, the heating/cooling processes of dust grains can inhibit fragmentation around protostars (Krumholz, Klein & McKee 2007; Bate 2009; Offner et al. 2009), and scaling this with metallicity can alter the density and temperature structure even in low-mass clusters (Bate 2019). When considering feedback from massive stars, changing the metallicity and dust fraction can modify the D-type expansion of H II regions. Haworth et al. (2015) investigated this with detailed photoionization modelling in 1D, with a single ionizing source in a uniform-density medium. Including dust grains resulted in the attenuation of ionizing radiation, which made the H II region smaller compared to the model without dust. A higher gas metallicity resulted in a lower electron temperature, decreasing the expansion rate of H II regions. Applying this in 3D to turbulent star-forming regions could provide key information for interpreting the observations that probe different metallicity environments.

Over the last decade and a half, there has been a growing body of work in 3D simulations of photoionization to investigate star formation and gas dynamics (including but not limited to Dale et al.

★ E-mail: A.Ali2@exeter.ac.uk

2005; Mellema et al. 2006; Peters et al. 2010; Arthur et al. 2011; Dale, Ercolano & Bonnell 2012; Walch et al. 2012; Colín, Vázquez-Semadeni & Gómez 2013; Geen et al. 2015; Howard, Pudritz & Harris 2016; Gavagnin et al. 2017; Ali, Harries & Douglas 2018; Kim, Kim & Ostriker 2018; Vandenbroucke & Wood 2019; Zamora-Avilés et al. 2019; Bending, Dobbs & Bate 2020; Fukushima et al. 2020; Sartorio et al. 2021). Models span a wide range of initial cloud conditions across mass, density, morphology, turbulence, and stellar population. In general, SFEs are reduced by the impact of photoionization compared to hydrodynamics-only runs, with some calculations showing only a modest reduction (e.g. Dale et al. 2014; Howard, Pudritz & Harris 2017) while others reach the low values seen in the Milky Way (e.g. Geen, Soler & Hennebelle 2017).

RP is now routinely included in models of massive star formation on the scale of individual cores (Krumholz et al. 2009; Kuiper et al. 2010; Harries, Douglas & Ali 2017; Rosen et al. 2019; Mignon-Risse et al. 2020) and implementations are becoming more common for the cluster/GMC scale. For example, RP has been investigated on its own (Skinner & Ostriker 2015; Tsang & Milosavljević 2018) and in conjunction with photoionization (Howard et al. 2016, 2017; Ali et al. 2018; Kim et al. 2018; Ali & Harries 2019; Fukushima et al. 2020). Overall, RP appears to be a secondary effect at the GMC scale, except possibly at the highest masses/luminosities/surface densities where it becomes more important (Fall, Krumholz & Matzner 2010; Howard, Pudritz & Harris 2018).

However, radiative transfer methods for photoionization are often simplified by prescribing a single temperature for ionized gas, using the on-the-spot approximation, or neglecting dust that absorbs UV radiation and reprocesses it into the infrared. Models that include RP typically only use ∼2 frequency bins (e.g. ionizing and non-ionizing photons), use an average dust opacity, and neglect the pressure from either direct (stellar) radiation or indirect (dust-processed) radiation, depending on the regime of interest. This does not accurately capture all the microphysics, as wavelength-dependent dust opacities span many orders of magnitude, and dust-processed radiation may undergo multiple absorption/re-emission/scattering events that can particularly affect high surface density gas (Crocker et al. 2018). Likewise, for photoionization, the presence of diffuse ionizing radiation and dust absorption can change the size and morphology of H II regions (Ercolano & Gritschneder 2011; Haworth & Harries 2012; Haworth et al. 2015). Furthermore, capturing the metallicity dependence of the electron temperature requires computing heating/cooling rates that take into account metal ions.

In previously published models (Ali et al. 2018; Ali & Harries 2019), we included these processes using a detailed Monte Carlo radiative transfer (MCRT) scheme for clouds of 10^3 and 10^4 M$_\odot$ and a single massive star. In this paper, we model a 10^5 M$_\odot$ cloud with $Z/Z_\odot = 0.1, 0.5, 1,$ and 2, with dust-to-gas ratio scaling linearly with Z. We have extended the method to track star formation using cluster-sink particles that form on the fly, accrete gas, and sample stars from an initial mass function (IMF). They emit photon packets from across the spectrum, which then propagate through gas/dust in the interstellar medium. We detail the numerical methods in Section 2, go through the results in Section 3, discuss them in Section 4, and conclude in Section 5.

2 NUMERICAL METHODS

We use the TORUS code, which couples MCRT with hydrodynamics on a 3D grid (for a full description of the code, see Harries et al. 2019). We use the same methods as Ali et al. (2018) and Ali & Harries (2019), with different initial conditions and the addition

Table 1. Abundances at solar metallicity (Asplund et al. 2009) and ion states used in the photoionization scheme.

Element	N_X/N_H	Ion states
Hydrogen	1	I–II
Helium	8.5×10^{-2}	I–III
Carbon	2.7×10^{-4}	I–IV
Nitrogen	6.8×10^{-5}	I–III
Oxygen	4.9×10^{-4}	I–III
Neon	8.5×10^{-5}	I–III
Sulphur	1.3×10^{-5}	I–IV
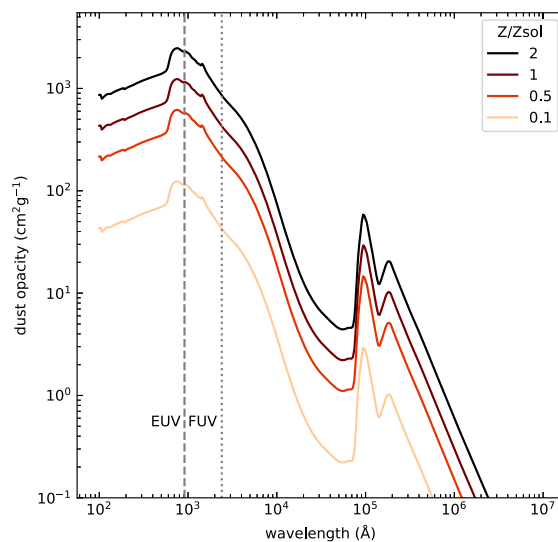
Figure 1. Dust opacities used in TORUS as a function of wavelength and metallicity (Z). Also marked are the upper limits of the extreme and far-ultraviolet (EUV and FUV, respectively).

of a cluster-sink particle approach detailed in Section 2.1. As a summary, the hydrodynamics scheme is flux conserving, finite volume, and total variation diminishing. Poisson's equation for self-gravity is calculated using a V-cycling multigrid method with Dirichlet boundary conditions based on a multipole expansion. Gas can flow out of the grid but not in. The hydrodynamics evolves isothermally, with temperatures set by an MCRT calculation at the beginning of each time-step. The MCRT scheme is based on the method of Lucy (1999). The source luminosity is split into photon packets that propagate through the medium, undergoing absorption/re-emission/scattering events until they exit the grid. Photoionization equilibrium is computed for the ion states listed in Table 1 using the method described by Haworth & Harries (2012), with abundances scaling linearly with metallicity. Photon wavelengths are interpolated from 1000 logarithmically spaced bins between 10^2 and 10^7 Å. The MCRT scheme therefore follows the diffuse radiation field as well as the stellar radiation field, including ionizing photons re-emitted by gas, and photons reprocessed by dust. The method naturally takes into account shadowed regions, penetration of shadows by diffuse radiation, and radiation hardening. We use Draine & Lee (1984) silicate grains with an MRN (Mathis, Rumpl & Nordsieck 1977) density distribution,

$$n(a) \propto a^{-3.5}, \qquad (1)$$

where the grain size a is between 0.005 and 0.25 μm. The dust opacity is plotted in Fig. 1. We do not include dust destruction,

as on GMC scales this occurs primarily through supernova shocks (Jones 2004). We assume the dust is dynamically well coupled to the gas. Elemental abundances at solar metallicity are taken from Asplund et al. (2009) and are listed in Table 1. Thermal balance between photon absorption and thermal emission provides the dust temperature. This is connected to the gas temperature by a collisional heat exchange rate from Hollenbach & McKee (1979),

$$\Gamma_{\text{gas–dust}} = 2 f n_{\text{H}} n_{\text{d}} \sigma_{\text{d}} v_{\text{p}} k_{\text{B}} (T - T_{\text{d}}), \tag{2}$$

where T_{d}, n_{d}, and σ_{d} are the dust temperature, number density, and cross-section, respectively, T is the gas temperature, v_{p} is the thermal speed of protons at T, and f is a factor that depends on T and the ionization fraction. The gas thermal balance uses heating rates from H and He photoionization, cooling from H and He recombination lines, collisionally excited lines from H and metals, and free–free continuum. This takes into account the frequency dependence of the stellar spectra and diffuse radiation field. The momentum-transfer method of Harries (2015) provides a value for the RP, which is added on to the momentum equation in the hydrodynamics step. We do not include magnetic fields in these models.

2.1 Cluster-sink particles

We use the sink particle algorithm described by Harries (2015) that uses formation criteria based on Federrath et al. (2010). Due to the spatial resolution of the calculations we present here, we do not follow the formation of individual stars; so we have extended the method to make sink particles represent clusters or subclusters. Sinks are formed above a density threshold of $10^4 \, \text{cm}^{-3}$, which corresponds to the density above which stars are observed to form in cores in the Galactic disc (Lada & Lada 2003; Barnes et al. 2019 and references therein; see also Howard, Pudritz & Harris 2014 who use this criterion with a similar method in their simulations).

Before starting the simulations, we pre-tabulate a list of stars by randomly sampling from a Chabrier (2003) IMF up to a total of $10^5 \, \text{M}_\odot$. This is similar to the method by Geen et al. (2018), but we retain the stars below $8 \, \text{M}_\odot$ as well. We use the same pre-tabulated IMF for every model. Each sink has a reservoir of mass available for star formation that is replenished by accretion on to the sink. The sink mass gets converted into a stellar population with an efficiency $\epsilon = 0.3$, such that the reservoir mass $M_{\text{reservoir}} = \epsilon M_{\text{sink}} - \sum M_*$, where M_* is the individual stellar masses in that sink. The value of ϵ is based on observational constraints from Lada & Lada (2003); the simulations by Howard et al. (2014) use a similar approach with an efficiency of 0.2 per free-fall time. After each hydrodynamical time-step, we check which reservoirs are massive enough to take the next star off the list and select one of those at random. The stellar mass is subtracted from the reservoir, and the process continues down the list until no sink reservoirs are massive enough.

While the position and velocity of each star simply follow the parent sink particle, other stellar properties including mass, radius, and luminosity vary independently with time. These evolve using interpolated values from the MESA Isochrones & Stellar Tracks (MIST; Choi et al. 2016) with rotational parameter ($v/v_{\text{crit}} = 0$) and metallicity [Fe/H] following the gas metallicity set in the initial conditions (Section 2.2). A sink is allowed to radiate after it is populated with a star more massive than $8 \, \text{M}_\odot$, with non-massive stars also contributing to the spectrum. A sink with *only* low-mass stars does not radiate, as the photoionization calculation is more stable without the ionizing flux, which is negligible but non-zero. Radiation is emitted from the sink particle as a point source, with the sink's luminosity being the sum of its component stellar luminosities ($L_{\text{sink}} = \sum L_*$),

Table 2. Model parameters.

Model	$Z \, (\text{Z}_\odot)$	Dust/gas	Ionization	RP
z2	2	0.02	✓	✓
z1	1	0.01	✓	✓
z0.5	0.5	0.005	✓	✓
z0.1	0.1	0.001	✓	✓
z1_norp	1	0.01	✓	✗
z1_norp_nodust	1	10^{-20}	✓	✗
hydro	n/a	n/a	✗	✗

and the sink's spectral energy distribution (SED) being an addition of its component stellar SEDs. SEDs for O stars are interpolated from the TLUSTY OSTAR2002 (Lanz & Hubeny 2003) grid of models using the relevant gas metallicity, while late-type stars use Kurucz (1993) models. In the next hydrodynamical step, the sink particle may continue accreting and the population procedure is repeated. Spectra are only recalculated every 10 hydrodynamical time-steps, as this reduces the computation time and the hydrodynamical time-scale is much shorter than the stellar evolutionary time-scale; however, a calculation is forced for sinks that have just been populated.

2.2 Initial conditions

Our initial condition is a spherical cloud with mass $M = 10^5 \, \text{M}_\odot$ and radius $R = 11.9 \, \text{pc}$. These parameters are based on observations of molecular clouds by Roman-Duval et al. (2010). The sphere has a uniform-density inner core up to $r = R/2$, then a power-law decrease with $\rho(r) \propto r^{-1.5}$. The density outside the sphere is $0.01\rho(R)$. The mean mass density and the number density of the sphere are $1.05 \times 10^{-21} \, \text{g cm}^{-3}$ and $629 \, \text{cm}^{-3}$, respectively. The free-fall time associated with this average density is $\langle t_{\text{ff}} \rangle = 2.1 \, \text{Myr}$. The mean surface density is $\Sigma = 0.05 \, \text{g cm}^{-3} = 240 \, \text{M}_\odot \, \text{pc}^{-2}$. The temperature is initially $10 \, \text{K}$ for both gas and dust. The grid size from end to end is $45.4 \, \text{pc}$, giving a linear resolution of $0.18 \, \text{pc}$ per cell with 256^3 cells. The grid structure is fixed, uniform, and Cartesian.

We investigate four metallicities, $Z/\text{Z}_\odot = 2$, 1, 0.5, and 0.1. For each metallicity, we assume a dust-to-gas mass ratio $= 0.01 \times Z/\text{Z}_\odot$ following Draine et al. (2007). For $Z = \text{Z}_\odot$, we carry out two more models to investigate the effects of RP and UV absorption: one with dust but no RP, and one with no dust and no RP. The models and their labels are summarized in Table 2. Metallicity and dust-to-gas ratio remain fixed over the simulation.

We apply a random Gaussian turbulent velocity field over the sphere. This is taken from Bate, Bonnell & Bromm (2002) and has a power spectrum $P(k) \propto k^{-4}$ for wavenumber k, such that the kinetic energy equals the gravitational potential energy, i.e. the virial parameter $\alpha_{\text{vir}} \equiv 2E_{\text{kin}}/E_{\text{grav}} = 2$. We check the criteria for sink particle formation, accretion, and star population as described in Section 2.1 at every time-step (unlike our previous models, Ali et al. 2018 and Ali & Harries 2019, where star particles were placed at $0.75 \langle t_{\text{ff}} \rangle$).

3 RESULTS

The spherical cloud evolves under self-gravity and a decaying turbulent velocity field. This creates filaments in which sink particles eventually form, especially in the inner half of the sphere where the density is highest. The first sink forms after $0.42 \, \text{Myr}$ ($0.2 \langle t_{\text{ff}} \rangle$). The first massive star ($19 \, \text{M}_\odot$) forms at $0.80 \, \text{Myr}$ ($0.38 \langle t_{\text{ff}} \rangle$) – beyond this point in the text and in all plots, we define this as $t = 0$
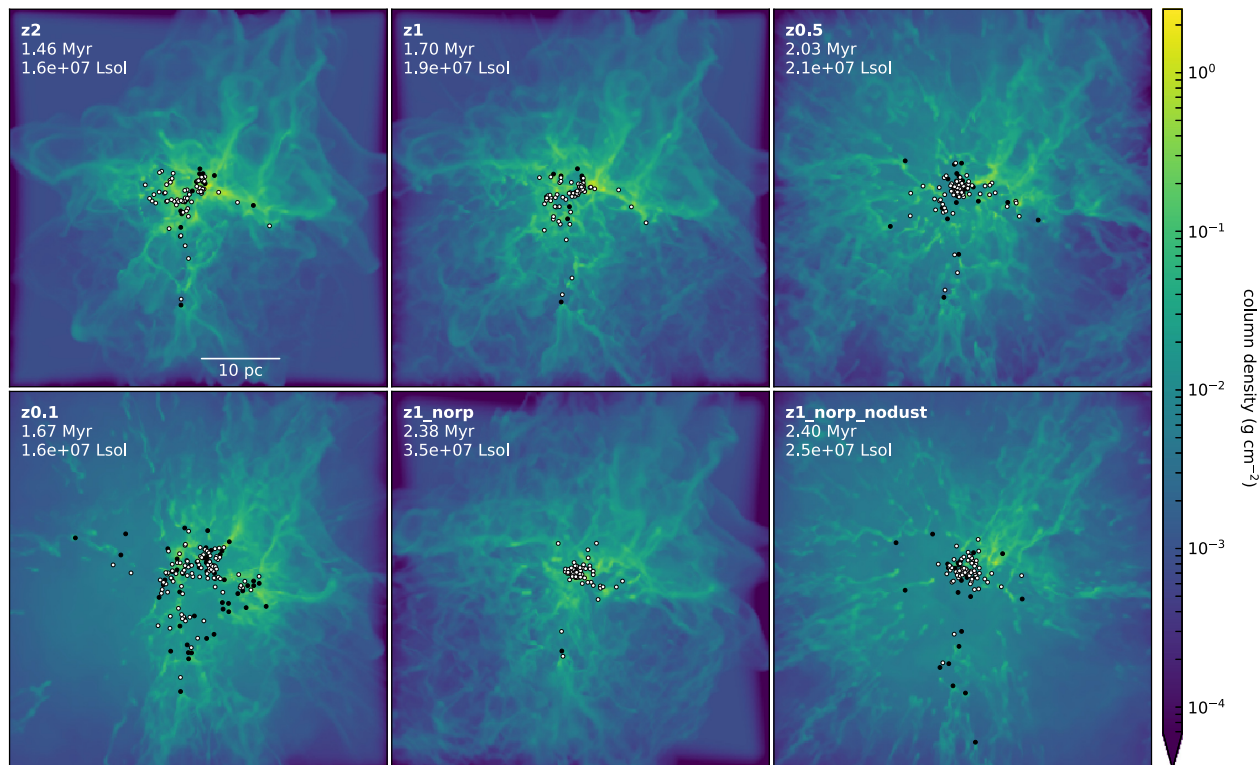
Figure 2. Final snapshots of column density (Σ) integrated along the z-axis. White dots show radiating sinks and black dots show non-radiating sinks. Labels show the model name, the time since the formation of the first massive star, and the total bolometric luminosity. The grid is 45.4 pc on each side.

as this is also when the radiative feedback starts. H II regions are created around sinks that accrete enough mass to form massive stars. As the H II regions expand, they collect gas into shells. Because the density structure is non-uniform, radiation is able to penetrate through lower density gas, ionizing areas of the cloud further away (including the diffuse environment outside the cloud). Individual H II regions also combine with neighbouring ones. Dense structures resist being ionized, but their star-facing surfaces get photoevaporated. The morphology of the gas and H II regions can be seen in Figs 2 and 3, which show the final snapshots of column density $\int \rho \, dz$ and emission measure $\int n_e^2 \, dz$, where ρ and n_e are the mass volume density and electron number density, respectively. Projected positions of sink particles are shown as circles, with white circles for radiating sinks (those which have massive stars $> 8\,M_\odot$) and black circles for non-radiating sinks (no massive stars). The five most massive stars in the z1 model were (in order of formation time), 78.5 $M_\odot$ (0.56 Myr), 97.8 $M_\odot$ (0.92 Myr), 103.5 $M_\odot$ (1.31 Myr), 88.0 $M_\odot$ (1.42 Myr), and 115.9 $M_\odot$ (1.69 Myr) at which point the computation ended. Simulations were stopped due to small time-steps caused by the acceleration from RP. In Section 3.1, we analyse the growth of the ionized gas as a function of time, and examine the kinematics of both the neutral and ionized components. In Section 3.2, we calculate star formation rates/efficiencies and cluster properties. Finally in Section 3.3, we compare the thermal pressure and RP to determine how each feedback mechanism contributes to the dynamics.

3.1 H II region expansion

The total ionized mass and volume as a function of time in each model is shown in Fig. 4. We count cells as being ionized if the ionization

fraction of hydrogen is greater than 0.9. The solid lines show the different metallicities, while the dashed line shows z1_norp and the dotted line shows z1_norp_nodust (see Table 2 for the parameters and physics in each model). Lower metallicity models grow larger H II regions – a lower cooling rate from metal ions results in a higher temperature, which produces a larger pressure gradient between ionized and neutral gas; furthermore, a lower dust-to-gas ratio means less attenuation of ionizing photons by dust. The mean electron temperatures that we find at each metallicity are 5.6×10^3 K at 2 $Z_\odot$, 8.2×10^3 K at 1 $Z_\odot$, 11×10^3 K at 0.5 $Z_\odot$, and 17×10^3 K at 0.1 $Z_\odot$ – this is the temperature averaged over the ionized volume then averaged over time. The effect of dust absorption and RP is seen in the difference between z1_norp_nodust, z1_norp, and z1. Of the three, z1_norp_nodust grows the largest – photoionization is the only feedback mechanism, but there is no shielding from dust. Adding dust (z1_norp) results in the smallest H II region, by an order of magnitude, as now there are dust grains that attenuate the ionizing photons. Enabling RP (z1) gives a result in the middle, showing that the additional pressure component from dust is not effective enough to counter the stunting caused by absorption. z0.5 has practically the same amount of ionized mass and volume as z1_norp_nodust, and z0.1 has the most of all the models. For illustrative purposes, we also plot Spitzer (1978) expansion profiles as a function of time t,

$$R_I(t) = R_S \left(1 + \frac{7 c_I t}{4 R_S} \right)^{4/7}, \tag{3}$$

where R_S is the Strömgren radius,

$$R_S = \left(\frac{3 Q_0}{4\pi n_e^2 \alpha_B} \right)^{1/3}, \tag{4}$$
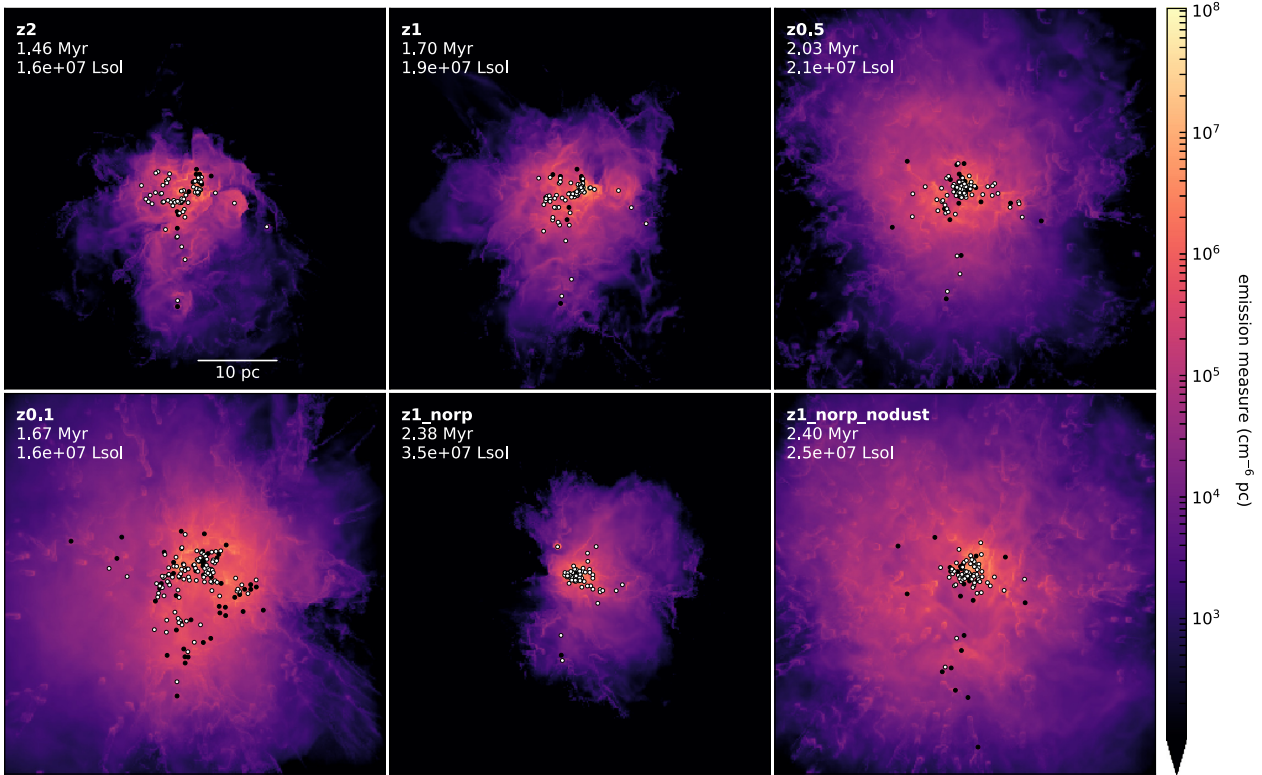
Figure 3. Final snapshots of emission measure $\int n_e^2 \, dz$. See also the caption of Fig. 2.

for three densities ($n_e = 10^2$, 10^3, and 10^4 cm^{-3}), using an ionizing photon production rate $Q_0 = 8 \times 10^{50}$ s^{-1}, which is the time-averaged rate for the longest-running model (z1_norp_nodust). The canonical temperature 10^4 K is used for the ionized sound speed (c_I), and the case B recombination coefficient ($\alpha_B = 2.7 \times 10^{-13}$ cm^3 s^{-1}). The Spitzer profiles are not meant to be exactly representative of the modelled H II regions, but they show that the variation between different models is similar to the variation between orders of magnitude in density.

We calculate the mass-weighted mean velocity in the radial direction,

$$\langle v_r \rangle = \frac{\sum_i m_i \boldsymbol{v}_i \cdot \hat{\boldsymbol{r}}}{\sum_i m_i} \tag{5}$$

summing over cells i with mass m_i and velocity $\boldsymbol{v}_i$ inside a radius of 10 pc around the simulation origin. $\hat{\boldsymbol{r}}$ is the unit vector pointing away from the origin. This is plotted in Fig. 5 for each model, separating out the neutral and ionized gas components. In both components, higher velocities belong to lower metallicities. Additionally, the two models without RP have smaller velocities than the other models, especially z1_norp (which has UV-attenuating dust and has the smallest H II region). The ionized gas is accelerated radially outwards for the entire duration of every model, with mean velocities reaching in excess of $+10$ km s^{-1} and still increasing as the models evolve. Velocities can be higher than the ionized sound speed as other dynamical mechanisms are involved, even in the ionization-only models – the surfaces of dense, neutral material can be photoevaporated, and this newly ionized gas can be accelerated to $\sim$30 km s^{-1} (see also Ali et al. 2018, where we show this in a lower mass cloud with a single massive star). An improvement on our previous models is that new sink particles form inside dense clumps and ionize them from the

inside, creating new compact H II regions. These expand and break out, joining up with H II regions formed by neighbouring sinks.

The neutral gas is infalling for the majority of the runtime for all models except z0.1 and (in the final 0.5 Myr) z0.5. Compared to the hydrodynamics-only run, the feedback models have slightly higher velocities (i.e. if gas is flowing inwards, it is doing so more slowly). Furthermore, the gradients eventually turn positive, showing that feedback is accelerating the neutral gas too. The hydrodynamics-only model is the only one that shows the rate of infall continually increasing. $\langle v_r \rangle$ for z1_hydro reaches a minimum value of -5.9 km s^{-1}, while the lowest velocity among the feedback models is -2.8 km s^{-1} – this is reached by z1_norp, which retains a constant infall velocity over its lifetime. z0.1, the most outflowing model, reaches a velocity of $+4.4$ km s^{-1}. Overall, feedback does affect the kinematics of the neutral gas, providing resistance against infall. However, z0.1 is the only model that exhibits neutral outflow for a significant period of the runtime. In addition to the support given by a higher thermal pressure against gravitational infall, neutral structures can experience a rocket effect when photoevaporated gas pushes off the surface (see also Mellema et al. 1998, 2006; Arthur et al. 2011), providing another source of acceleration not present in the hydrodynamics-only model.
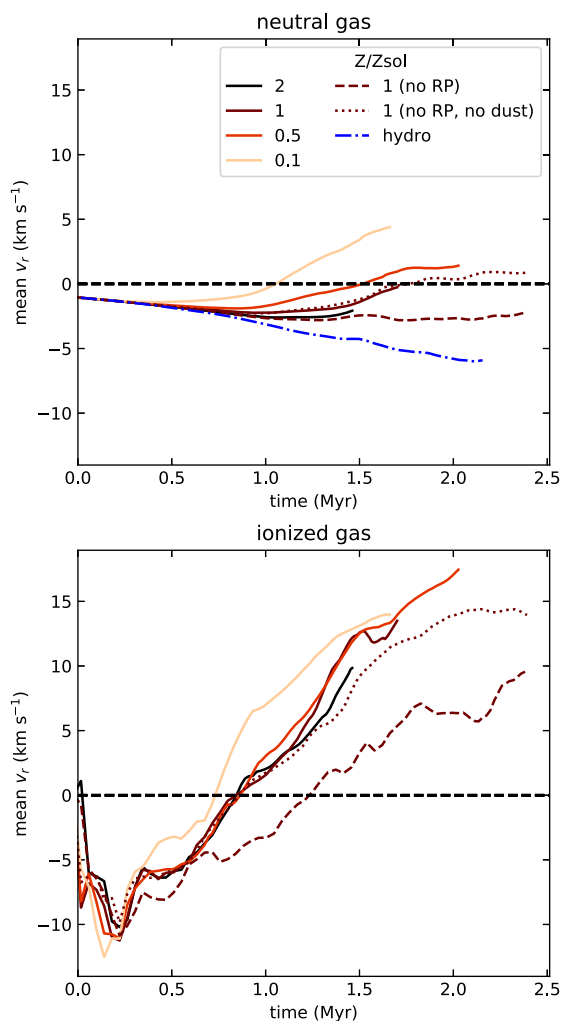
3.2 Star formation

Our cluster-sink method allows particles to form and accrete on the fly, which is an improvement on our previous method of placing individual stars manually at one pre-defined moment in time. The drawback is that a particular sink's stars are all lumped together into a point – instead of having many 1000s of real star particles, we have $\sim$100 'cluster' particles. While this provides a clear computational advantage, it makes it difficult to separate the ensemble of particles
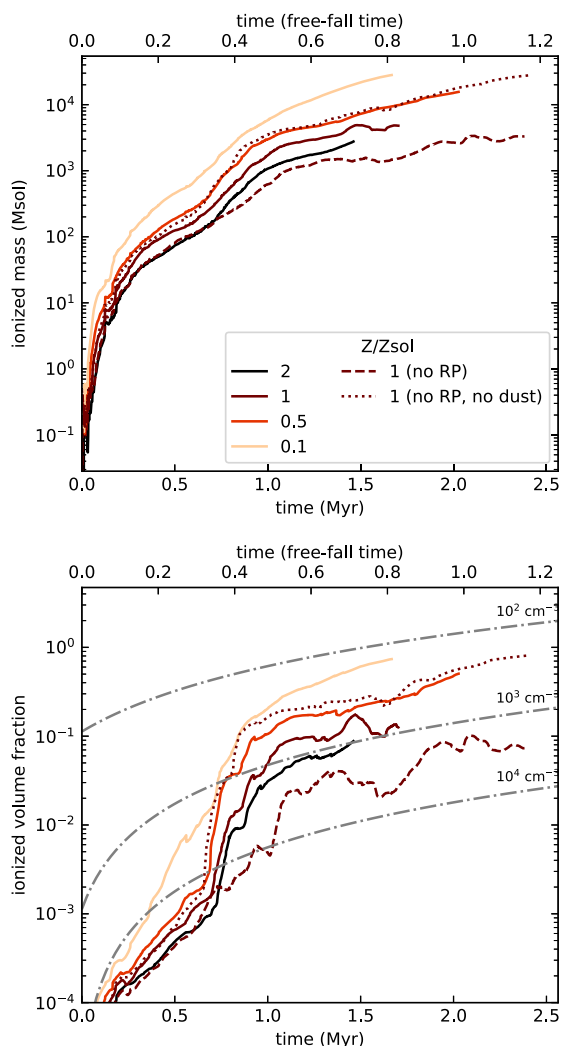
Figure 4. H II region properties – the top panel shows total ionized mass. The bottom panel shows total ionized volume as a fraction of the total grid volume (45.4^3 pc^3). The bottom plot also shows Spitzer expansion profiles (dot–dashed lines) for three densities ($n_e = 10^2$, 10^3, and 10^4 cm^{-3}, going downwards; see text for more detail). Times in all figures are since the formation of the first massive star and initiation of feedback.


Figure 5. Mass-weighted mean radial velocity in a sphere of radius of 10 pc around the simulation centre. Positive values indicate outflowing gas, negative values show infalling gas.

into several well-defined, distinct clusters, and to analyse individual clusters by themselves. For this reason, our analysis treats the whole system as one cluster.

Fig. 6 shows the evolution of the cluster half-mass radius (r_{hm}) versus total stellar mass for each model. In this case, 'cluster' means all sinks that are populated with at least one star, and the relevant mass is the stellar mass not the sink mass (see Section 3.2 for details about the sink particle method). r_{hm} is the radius from the centre of mass that encloses half the total mass. For comparison, we also show data for young massive clusters (YMCs) in the Milky Way and LMC from Portegies Zwart, McMillan & Gieles (2010). All the clusters lie between the Milky Way YMCs. With the exception of z0.1, all the models are indistinguishable from one another and become more compact as mass (i.e. time) increases, especially as they approach 10^4 M$_\odot$. Similar behaviour is seen by Liow & Dobbs (2020) in models of cloud–cloud collisions that do not include feedback, where massive clusters contract once gravity becomes important. The results imply that variations in metallicity, dust absorption, and RP do not guarantee changes in cluster compactness, even though the

H II regions produced by each model are of different sizes and masses (as shown in Fig. 4) – for example, z1_norp has the smallest H II region, while both z1_norp_nodust and z0.5 have an ionized volume which is an order of magnitude larger. That is, a larger H II region does not guarantee a larger cluster. z0.1 is an outlier as its cluster does not contract as much as the other feedback models, which all follow the same relationship as each other. This is because the neutral gas has a higher mean velocity, which is directed radially outwards for z0.1 instead of radially inwards as in the other models (see Fig. 5). Since the turnover from infall to outflow occurs relatively early in the evolution (by $t = 1$ Myr $= 0.5 \langle t_{ff} \rangle$), this halts the collapse of the gas and hence the sinks – the turnover happens too late (or not at all) for the other models. The hydrodynamics-only calculation is shifted to the right as it accretes more mass, due to the lack of pressure support from feedback and the accelerating rate of neutral-gas infall.

Fig. 7 shows the total accretion rate summed over all sink particles,

$$\dot{M}_{\rm sink,tot} = \sum \frac{\Delta M_{\rm sink}}{\Delta t}, \tag{6}$$

where Δt is the hydrodynamical time-step. The result is processed through a 3σ Gaussian filter to smooth some of the variation and show the trend more clearly. Fig. 7 also shows the SFE over all sink
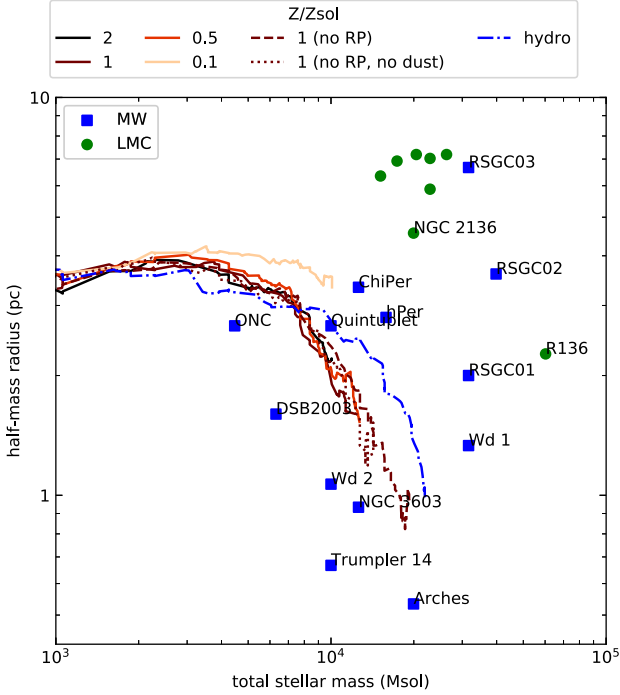
Figure 6. Cluster half-mass radius versus total stellar mass (which increases with time). For comparison, the plot also shows YMCs observed in the Milky Way and LMC (Portegies Zwart et al. 2010).

particles relative to the initial cloud mass,

$$\mathrm{SFE} = \frac{\sum M_*}{10^5 \, \mathrm{M}_\odot}. \tag{7}$$

Sink accretion rates lie around $10^{-2} \, \mathrm{M}_\odot \, \mathrm{yr}^{-1}$ for the majority of the runtime, with the hydrodynamics-only run being consistently higher than the feedback models by a factor of a few to 10 at most. The SFE does not exceed 20 per cent within a free-fall time except for the hydrodynamics-only model. The different metallicities cannot be easily distinguished, although they show signs of deviating from each other approximately $0.6 \langle t_{\mathrm{ff}} \rangle$ after the first massive star is formed. Of the models that run the longest, z1_norp (dashed line) has a higher SFE than z1_norp_nodust (dotted line) – 0.2 versus 0.15. The former has a smaller H II region (Fig. 4) and smaller radial expansion velocities both for ionized gas and neutral gas (Fig. 5), meaning more mass can funnel into sink particles, creating more stars; the sink accretion rate for this model is higher by about a factor of 10 at late times. Overall the differences between the feedback and hydrodynamics runs are modest, with the hydrodynamics model having approximately 1.5–2 times greater SFE. Higher metallicity results in higher accretion rates and SFEs, although we stress the deviation at this stage is marginal.
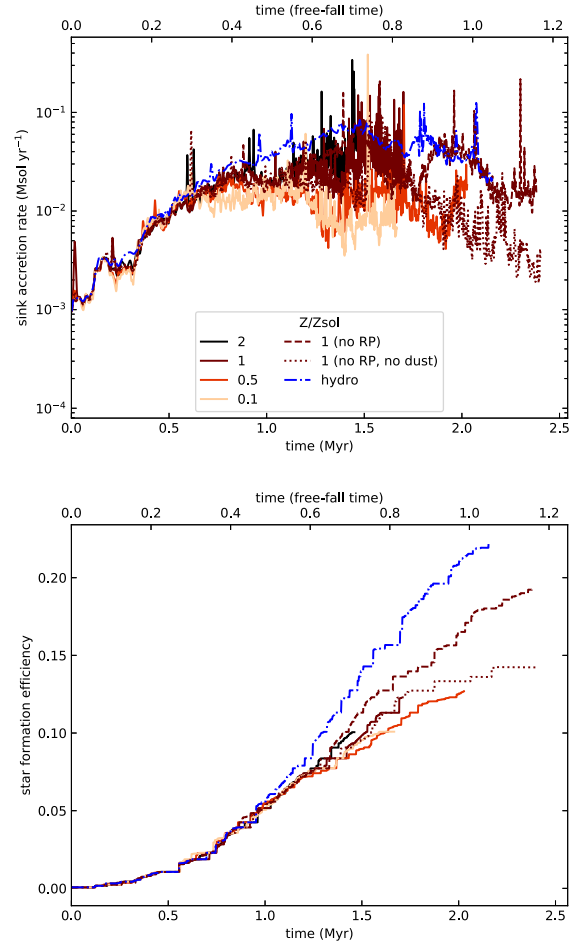
3.3 Pressure contributions

In this section, we calculate the RP as the magnitude of the radiative force per unit area

$$P_{\mathrm{rad}} = |\boldsymbol{f}_{\mathrm{rad}}| \Delta x, \tag{8}$$

where $\boldsymbol{f}_{\mathrm{rad}}$ is the force per unit volume as calculated in the MCRT step, and Δx is the cell size. The thermal pressure is given by the ideal gas equation of state

$$P_{\mathrm{gas}} = \frac{\rho k_B T}{\mu m_H}, \tag{9}$$

Figure 7. Sink accretion rate (top) and SFE (bottom).

where ρ is mass density, k_B is Boltzmann's constant, T is temperature, μ is the mean molecular weight, and m_H is the hydrogen mass. Fig. 8 shows a zoomed-in snapshot of the z1 model, plotting the mean P_{rad} along the line of sight, the mean P_{gas}, and the ratio of the means. This focuses on the inner 7 pc around the cluster centre of mass at $t = 1.47 \, \mathrm{Myr}$. These projections are analogues of what can be inferred from observations (such as in Lopez et al. 2011; Pellegrini et al. 2011; although see caveats in Section 4.1). The region is, on the whole, dominated by the thermal pressure from ionization. RP is only significant near the sink particles. For example, the figure shows an area in the H II region that is dominated by RP, to the bottom right of the centre of mass (the cross symbol). This is where several sink particles are concentrated near a neutral, high-density clump. Additionally, a lone sink particle near the right edge of the frame is growing its own compact H II region and RP bubble. To characterize these pressure hotspots and identify trends as a function of radius, we also calculate radial averages of P_{gas}, P_{rad}, and the ratio $P_{\mathrm{rad}}/P_{\mathrm{gas}}$. To do this, we compute each quantity in every cell, bin it according to distance from the origin, then find the median, first quartile, and third quartile in each radial bin. This creates a series of concentric shells around the origin, with average values being found for each shell. These results are shown in Fig. 9.

The origin of the first column of Fig. 9 is the first H II region at $t = 0.43 \, \mathrm{Myr}$. The ionizing sources are the same in each model and have masses of 31.7, 27.8, and 18.7 $\mathrm{M}_\odot$. The H II region is approximately 2 pc in radius. In the innermost radial bins, $P_{\mathrm{rad}}/P_{\mathrm{gas}}$
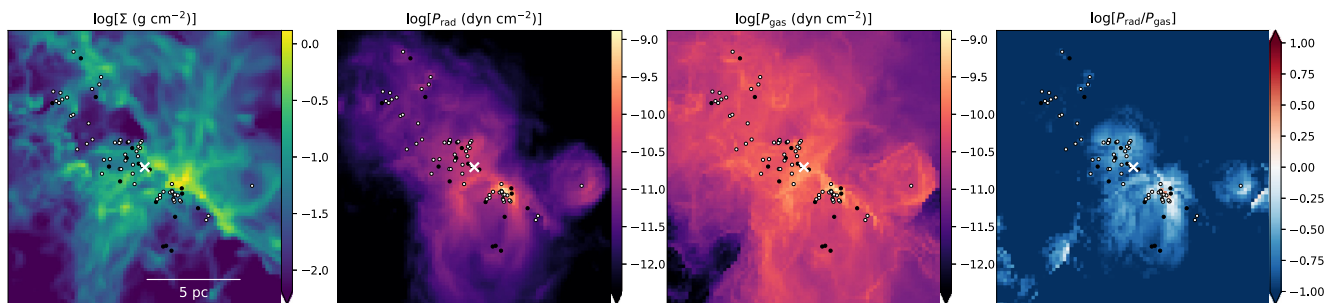
Figure 8. Zoomed-in snapshot showing an RP-dominated region in the z1 model at $t = 1.47$ Myr. P_{rad} and P_{gas} are the mean values integrated along the line of sight; the final frame is the ratio of the mean pressures. Images are centred on the cluster centre of mass (shown with an ×), with sink particle positions plotted as circles (using the same colour scheme as Fig. 2). These projections are integrals along the y-axis, not the z-axis as in Figs 2 and 3.

has values around 10 for the z2 model, 3 for z1, 1 for z0.5, and 0.1 for z0.1. That is, RP dominates over (or is at least comparable to) the gas pressure for all but the lowest metallicity case. This drops off with radius, with all metallicities having $P_{\text{rad}}/P_{\text{gas}} < 1$ by 0.7 pc.

The origin of the second column of Fig. 9 is the cluster centre of mass at $t = 1.22$ Myr. $P_{\text{rad}}/P_{\text{gas}}$ is approximately constant in the inner 5 pc, before tailing off at the ionization front. The median is just below 1 for z2, around 0.3 for z1, 0.1 for z0.5, and 0.03 for z0.1. The smaller ratio at low metallicity is caused by a combination of P_{rad} being smaller (lower dust-to-gas ratio) and P_{gas} being higher (higher temperature).

In summary, RP can be important at subpc scales near sink particles, while ionization becomes the dominant term further out. On the cluster scale, RP is at best comparable to the gas pressure ($Z \geq Z_\odot$), and at worst negligible ($Z = 0.1 Z_\odot$). For the z1 model, the total ionized mass and volume are larger when RP is enabled compared to when it is switched off (see Fig. 4). This can be caused by the high P_{rad} in the vicinity of sink particles clearing material away with a similar force as the thermal pressure from ionization. However, as explained in Section 3.1, a more effective way of producing a larger H II region is to remove the dust altogether; even though this removes the source of RP, it means more ionizing photons are absorbed by gas rather than processed away by dust – feedback is more efficient when photons are ionizing gas instead of imparting momentum to dust.

4 DISCUSSION

4.1 Comparison of pressures with observations

In this subsection, we compare the pressure contributions with observational studies of the LMC, SMC, and more recently of the Galactic Centre in the Milky Way. These regions have different metallicities, with $Z \approx 2$ in the Galactic Centre, $0.5 Z_\odot$ in the LMC, and $0.2 Z_\odot$ in the SMC (Russell & Dopita 1992; Deharveng et al. 2000). First, we consider the different definitions used in the literature. Lopez et al. (2011, 2014) define the direct RP as

$$P_{\text{dir}}(r) = \sum \frac{L_{\text{bol}}}{4\pi r^2 c}, \tag{10}$$

where the sum is over stars with bolometric luminosity (L_{bol}) at a projected distance (r) away from the point of interest, and c is the speed of light. The volume-averaged value is defined as

$$\langle P_{\text{dir}} \rangle = \frac{\int P_{\text{dir}}(r)\, dV}{\int dV} = \frac{3 L_{\text{bol}}}{4\pi R^2 c}, \tag{11}$$

where R is the radius of the H II region (or aperture). McLeod et al. (2019) and Barnes et al. (2020) use a similar expression, except they

assume $L_{\text{bol}} \approx Q_0 \langle h\nu \rangle$, the rate of ionizing photons emitted by the source population multiplied by the mean SED energy. It is important to note that this does not have a dependence on gas/dust properties (density, opacity, metallicity, etc). Therefore, as noted by the authors, these expressions are strictly a property of the radiation field – they show the radiative momentum flux at position r given a luminosity which only decreases by geometric dilution. This is delivered as momentum in the gas if radiation streams through an optically thin medium before getting absorbed at the position r. Beyond r, the deposited momentum would be further reduced by attenuation. Alternatively, radiation could leak out through holes in the density structure instead of interacting with gas at all. Determining this observationally is made more complicated by projecting stars and gas to 2D. In short, this P_{dir} measures the *potential* for a source to provide momentum, not how much momentum is actually deposited in the gas. Without accounting for density, it is possible that P_{dir} is being overestimated in the observations, particularly for larger radii/optical depths, as P_{dir} is propagating as $\propto r^{-2}$ instead of $\propto r^{-2} e^{-\tau(r)}$. Pellegrini et al. (2011) use a different method, carrying out a grid of CLOUDY (Ferland et al. 1998) photoionization models for varying positions (r) and densities (n_{H}; keeping Q_0 fixed). Therefore, instead of equation (10), they have

$$P_{\text{dir}}(r) = \left(\frac{Q_0}{4\pi r^2 c n_{\text{H}}} \right) n_{\text{H}} \langle h\nu \rangle \frac{L_{\text{bol}}}{L_{\text{ion}}}, \tag{12}$$

where the term in brackets is the best-fitting output of the photoionization models, and L_{ion} is the ionizing luminosity. This does take into account some of the density and positional information of the source and H II region.

With these caveats, we can compare with the trends found by Lopez et al. (2011; equation 10) and Pellegrini et al. (2011; equation 12) who both observed 30 Doradus in the LMC and computed pressure ratios at multiple points inside the region. Both studies found that the direct RP was greater than or comparable to the ionized gas pressure in the inner region, but was less important further out, by up to an order of magnitude. However, they disagree about the distances involved – Pellegrini et al. (2011) say RP dominated the inner 10 pc, while this is closer to 70 pc for Lopez et al. (2011). The maximum of $P_{\text{dir}}/P_{\text{gas}}$ was around 3 for Pellegrini et al. (2011) and 10 for Lopez et al. (2011); the discrepancies may be attributed to differences in the method. Compared with our models, 30 Doradus is an extreme example containing stars with higher luminosities and effective temperatures (thus more energetic spectra). This makes the RP larger, as $P_{\text{dir}} \propto L_{\text{bol}} \propto T_{\text{eff}}^4$. The ratio $P_{\text{dir}}/P_{\text{gas}}$ is similarly affected, as the ionized gas temperature (T) does not scale significantly with T_{eff} (and $P_{\text{gas}} \propto T$).
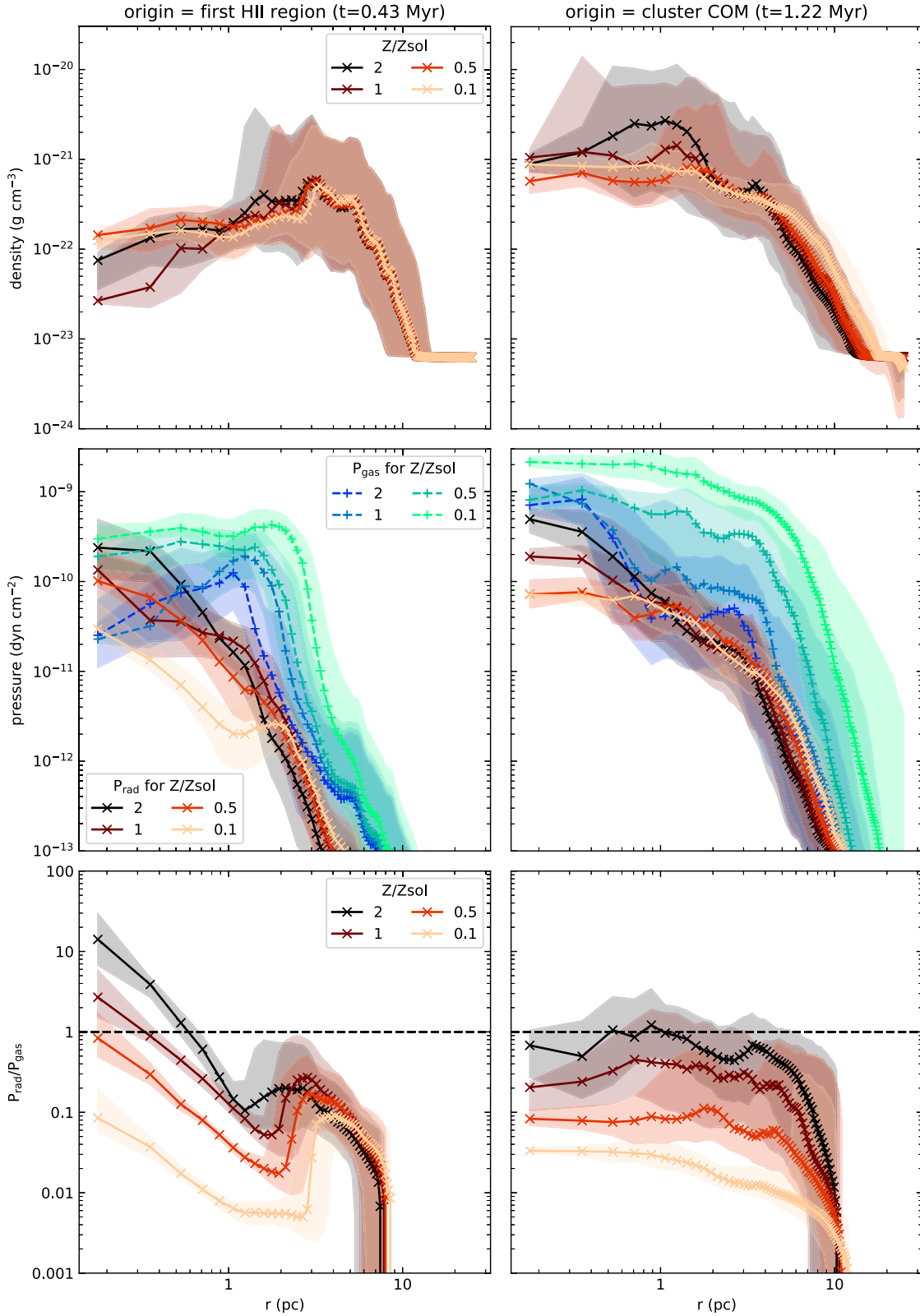
Figure 9. Radial profiles of density, gas thermal pressure (P_{gas}), RP (P_{rad}), and the ratio (P_{rad}/P_{gas}). Points show the median value in each radial bin. Filled regions show the first and third quartiles in the bin. The origin for the left-hand column is the first massive star H II region. The right-hand column has the origin at the cluster centre of mass.

A later study by Lopez et al. (2014) examined 32 H II regions in the LMC and SMC using volume-averaged pressures (equation 11). They found that the ionization pressure was the dominant term, while the direct RP was up to two orders of magnitude smaller (~few

$\times\, 10^{-12}\,\mathrm{dyn\,cm^{-2}}$). These results were consistent across H II region sizes between 10 and 100 pc. McLeod et al. (2019) observed LMC H II regions with higher angular resolution and identified younger, more compact subregions (down to 3 pc). They reached similar

conclusions to Lopez et al. (2014), although values of $\langle P_{\mathrm{dir}} \rangle$ were even smaller (by a factor of 10) which they attribute to the method being dependent on morphology. Barnes et al. (2020) examined H II regions in the supersolar metallicity of the central molecular zone (CMZ) of the Milky Way. The authors note that the CMZ has higher ambient pressures than the LMC/SMC, which would affect the expansion of the H II region and the point where pressure equilibrium between ionized gas and neutral gas is reached (see Raga, Cantó & Rodríguez 2012 for the theoretical description). They used equation (11) that is not metallicity-dependent, but the thermal gas pressure (and hence the ratio between them) is, as $P_{\mathrm{gas}} \propto T$. For a sample of H II regions up to a few pc in size, they found a trend with radius showing the direct RP was dominant up to 0.1 pc, beyond which the ionization pressure became important. The largest ratios were reached on the smallest scales within Sgr B2, with $P_{\mathrm{dir}}/P_{\mathrm{gas}} \approx 10$.

A final note can be made on the role of the indirect RP. Although our models do include both components, they cannot be disentangled explicitly as we track the *net* momentum change in each cell, not the momentum transferred with each photon interaction event – in the notation of the observational papers, our $P_{\mathrm{rad}} = P_{\mathrm{dir}} + P_{\mathrm{IR}}$. The observational studies that calculate both components show one of them being much larger than the other. Lopez et al. (2014) found $P_{\mathrm{IR}} \sim 0.1 P_{\mathrm{gas}}$ ($\sim$few $\times 10^{-11}$ dyn cm^{-2}), except for two sources where they were comparable, and $P_{\mathrm{IR}} \gg P_{\mathrm{dir}}$. Conversely, Lopez et al. (2011) found $P_{\mathrm{IR}} \ll P_{\mathrm{dir}}$. Therefore, it seems reasonable to compare our P_{rad} to whichever component is dominant for a particular region. A more analogous comparison could be made by computing synthetic observations from our simulations and using the observational methodology on those outputs. In summary, our work is broadly in agreement with the observational results – if RP is the dominant feedback mechanism, this occurs at small scales, while the thermal pressure dominates on larger scales.

4.2 Comparison with theory

Our SFE results are almost the same for each metallicity, although it is possible they may diverge were the models to be evolved for longer. Fukushima et al. (2020) did find differences as a function of metallicity in their models of photoionization and RP at $Z/Z_{\odot} = 1$, 0.1, and 0.01. They found lower SFEs at lower metallicities, attributing this to the greater disruption at higher temperature. For a similar surface density as our model, the different metallicities showed SFEs of around 20 per cent at 1 $Z_{\odot}$, 10 per cent at 0.1 $Z_{\odot}$, and 3 per cent at 0.01 $Z_{\odot}$. The SFE was set by photoionization – the fiducial model with both mechanisms was the same as the model with only photoionization, while the model with only RP had a greater SFE by a factor of 4 (a more drastic variation than we find).

Kim et al. (2018) also found that RP was secondary to photoionization in their parameter study of GMC mass and surface density. In particular, RP started to become important above 200 $M_{\odot}$ pc^{-2} (for reference, our cloud is 240 $M_{\odot}$ pc^{-2}). In general, lower SFEs were reached by photoionization-only models compared to RP-only runs, and combined-feedback models were slightly lower; around this surface density, the SFEs were around 20–40 per cent. It should be noted that Kim et al. convert 100 per cent of the sink mass to stars, while we limit this to 30 per cent. As in our models, the ratio between the hydrodynamics and feedback SFE was around 0.5.

Howard et al. (2017) also carried out combined photoionization–RP simulations. They saw SFEs around 16–21 per cent in GMCs between 10^4 and 10^6 $M_{\odot}$, which are only slightly higher than the results we find here (albeit their simulations are evolved for a longer fraction of the free-fall time). The reductions in the SFE compared

with hydrodynamics-only runs were 20–50 per cent, which are also exhibited by longer running models in our set of simulations. Their star formation method and definition of the SFE are similar to ours, perhaps making this a more direct comparison than with Kim et al. (2018). Howard et al. (2018) also applied the two mechanisms in a 10^7 $M_{\odot}$ cloud at $Z/Z_{\odot} = 1$ and 0.1. RP drove an outflow bubble around the central cluster, but only in the solar metallicity cloud. On those scales, photoionization was insignificant, with the SFE being the same as the hydrodynamics model when RP was switched off. They found the SFE at 0.1 $Z_{\odot}$ was higher than the solar model by a factor of 4, which is the opposite trend to Fukushima et al. (2020). However, Howard et al. only emitted radiation from sink particles once they exceeded 10^4 $M_{\odot}$, and this could affect the evolution at early times.

The right-most panel of Fig. 8 shows a region of high RP where gas is accelerated in the cells around a dense group of sink particles. This creates a cavity in the ionized gas at this location, comparable to the descriptions by Mathews (1967) and Draine (2011). It should be noted that dust is dynamically well coupled to the gas in our numerical scheme. Taking into account separate dust dynamics can result in a dust cavity with variations in dust-to-gas ratio and grain size distribution, as well as shallower gradients in gas density (Akimkin et al. 2015, 2017; Ishiki, Okamoto & Inoue 2018).

Variation in the initial conditions between simulations clearly adds complexity when trying to make direct comparisons – the structure of the density and velocity before stars form and feedback initiates will affect cloud evolution. In addition to mass, average density, and radial dependence of density, different models use different turbulent velocity fields. The effects of this were investigated by Geen et al. (2018), who carried out a suite of models with photoionization feedback, varying the velocity structure and hence final cloud length and filamentary structure. Separately, they varied the random sampling of the IMF in the star formation prescription. Resulting SFEs varied between 6 and 23 per cent, showing that a relatively large margin of error can be caused by the model set-up and not just the feedback physics. In the context of those results, our work would imply that variations in metallicity are not as important as other initial conditions such as morphology when it comes to setting the SFE.

Radial velocities for Kim et al. (2018) were between +18 and +26 km s^{-1} for ionized gas, and between +5 and +15 km s^{-1} for neutral gas. The magnitudes are similar to our results, particularly for the lowest metallicity model, and are consistent with the rocket effect (Oort & Spitzer 1955; Mellema et al. 1998, 2006; Arthur et al. 2011). The fact that feedback in our clouds must first overcome infall could be due to the initial radial density profile – Kim et al. (2018) use clouds with uniform density, while ours are centrally concentrated. The RP-only model by Tsang & Milosavljević (2018) shows infall being stabilized by feedback to a near-constant velocity, while the hydrodynamics run collapses at an accelerating pace. Again, the initial conditions differ, as Tsang & Milosavljević (2018) use a turbulent box with 100 times more mass and 30 times the density of our cloud, so the infall velocities were also faster – inside a 1 pc radius around the central cluster, this approached -100 km s^{-1} after a free-fall time in the hydrodynamics run, and around -20 km s^{-1} in the feedback case. None the less, the qualitative behaviour matches what we find.

Our general results show that photoionization is the dominant feedback mechanism driving the evolution of the cloud, while RP plays a secondary, local role. This is similar to the dichotomy between photoionization and momentum-only stellar winds as described by Dale et al. (2014), where the momentum injected by winds created cavities around sink particles. Likewise, our SFEs are higher than expected for the GMC scale, which could be attributed to the initial

conditions, or to the lack of other feedback mechanisms (such as energy-injecting stellar winds and supernovae that produce hot gas around $\sim 10^6$ K). While there is still uncertainty about the impact of metallicity on star formation, its role in gas dispersal is clearer – lower metallicity aids photoionization, while higher metallicity aids RP.

5 SUMMARY AND CONCLUSIONS

We have modelled a $10^5\,M_\odot$ turbulent cloud with different gas metallicities, $Z/Z_\odot = 2, 1, 0.5$, and 0.1, and dust-to-gas ratio scaling linearly with Z. We included stellar feedback from cluster-sink particles in the form of photoionization and RP. We also computed thermal balance to consistently calculate electron temperatures at the different metallicities. We used an MCRT method that is able to capture the microphysical detail in each feedback mechanism – photon packets spanning orders of magnitude in wavelength interact with gas and dust grains in the same way as real photons, getting absorbed, reprocessed, and scattered. This presents a key advancement compared to previous studies of stellar feedback in GMCs. The method provides robust calculations of ionization pressure, RP, and hence the ratio between them. As these quantities are used to observationally constrain the relative importance of different feedback mechanisms (e.g. as a function of radius), it is necessary for simulations to provide accurate results. Our key findings are the following:

(i) Lower metallicity H II regions have higher temperatures and therefore expand faster. This is because metal forbidden lines are the dominant cooling mechanism for ionized gas. Temperatures range from 5.6×10^3 K at $2\,Z_\odot$ to 17×10^3 K at $0.1\,Z_\odot$.

(ii) Feedback disperses ionized gas and provides support against gravitational infall for neutral gas. Ionized gas is accelerated outwards for the entire duration of each model – the mass-weighted mean expansion velocity, $\langle v_r \rangle$, approaches $+15\,\mathrm{km\,s^{-1}}$ by the end of the simulations. Neutral gas has $\langle v_r \rangle$ directed inwards for most of the evolution. The pure hydrodynamics run is the only model where infall accelerates, reaching $\langle v_r \rangle = -5.9\,\mathrm{km\,s^{-1}}$. For the feedback models, the most negative $\langle v_r \rangle$ is $-2.8\,\mathrm{km\,s^{-1}}$ – the velocity either stabilizes or turns into outflow. This happens in the first Myr ($0.5\,\langle t_{\mathrm{ff}} \rangle$) at $0.1\,Z_\odot$, which by the end of its runtime has neutral gas flowing out at $+4.4\,\mathrm{km\,s^{-1}}$.

(iii) Switching off RP results in a smaller H II region than the fiducial model with both photoionization and RP (at solar metallicity).

(iv) However, switching off RP *and* removing dust results in an H II region *larger* than the fiducial one. This is because UV photons are absorbed by dust grains and reprocessed to lower energies, diluting the ionizing flux. In terms of H II region size, the growth caused by RP is not enough to completely offset the stunting caused by UV absorption. This highlights the importance of including dust radiative transfer in models of photoionization feedback, whether or not RP is included.

(v) We calculate the radial dependence of each pressure component. RP dominates over the gas pressure, or is at least comparable to it, in the inner 0.7 pc around sink particles for $Z \geq 1\,Z_\odot$. The maximum ratio of the RP to gas thermal pressure is $P_{\mathrm{rad}}/P_{\mathrm{gas}} \approx 10$ at $Z = 2\,Z_\odot$.

(vi) On the global scale, $P_{\mathrm{rad}}/P_{\mathrm{gas}}$ is around 1 at $2\,Z_\odot$, 0.3 at $Z_\odot$, 0.1 at $0.5\,Z_\odot$, and 0.03 at $0.1\,Z_\odot$.

Our results show that although RP is less important than photoionization on large scales ($\sim 10\,\mathrm{pc}$), it still aids in the growth of H II regions via RP hotspots on small scales ($< 1\,\mathrm{pc}$), especially above solar metallicity. This can explain differences in the observations,

where Lopez et al. (2014) and McLeod et al. (2019) infer negligible RP in H II regions larger than 3 pc at low metallicity, whereas Barnes et al. (2020) estimate RP is dominant on the subpc scale at high metallicity. To fully understand how the feedback processes affect the dynamics, it is necessary to observe pressure contributions in young and compact H II regions, in addition to the older, larger H II regions that have until recently been the primary focus of observational studies. Furthermore, this shows the metallicity dependence of RP must be taken into account, which is not yet apparent in the literature.

Our models specifically investigate the impact of metallicity and dust in radiative feedback, so we keep the same initial cloud conditions for all models. We do not take into account environmental factors such as variations in external pressure (Barnes et al. 2020) or galactic-scale forces (Rey-Raposo et al. 2017; Bending et al. 2020) that can influence the evolution of H II regions and GMCs. We use the same turbulent velocity field for each model and the same ordering of stars that populate cluster-sink particles; varying either can affect cloud morphology and star formation measures (Geen et al. 2018). Finally, we neglect other feedback mechanisms such as stellar winds, which may be needed to attain lower SFEs.

DATA AVAILABILITY

The data underlying this paper will be shared on reasonable request to the corresponding author.

REFERENCES

Akimkin V. V., Kirsanova M. S., Pavlyuchenkov Y. N., Wiebe D. S., 2015, MNRAS, 449, 440
Akimkin V. V., Kirsanova M. S., Pavlyuchenkov Y. N., Wiebe D. S., 2017, MNRAS, 469, 630
Ali A. A., Harries T. J., 2019, MNRAS, 487, 4890
Ali A., Harries T. J., Douglas T. A., 2018, MNRAS, 477, 5422
Arthur S. J., Henney W. J., Mellema G., de Colle F., Vázquez-Semadeni E., 2011, MNRAS, 414, 1747
Asplund M., Grevesse N., Sauval A. J., Scott P., 2009, ARA&A, 47, 481
Astropy Collaboration, 2013, A&A, 558, A33
Barnes A. T. et al., 2019, MNRAS, 486, 283
Barnes A. T., Longmore S. N., Dale J. E., Krumholz M. R., Kruijssen J. M. D., Bigiel F., 2020, MNRAS, 498, 4906
Bate M. R., 2009, MNRAS, 392, 1363
Bate M. R., 2019, MNRAS, 484, 2341

Bate M. R., Bonnell I. A., Bromm V., 2002, MNRAS, 332, L65
Bending T. J. R., Dobbs C. L., Bate M. R., 2020, MNRAS, 495, 1672
Chabrier G., 2003, PASP, 115, 763
Choi J., Dotter A., Conroy C., Cantiello M., Paxton B., Johnson B. D., 2016, ApJ, 823, 102
Colín P., Vázquez-Semadeni E., Gómez G. C., 2013, MNRAS, 435, 1701
Crocker R. M., Krumholz M. R., Thompson T. A., Baumgardt H., Mackey D., 2018, MNRAS, 481, 4895
Dale J. E., 2015, New Astron. Rev., 68, 1
Dale J. E., Bonnell I. A., Clarke C. J., Bate M. R., 2005, MNRAS, 358, 291
Dale J. E., Ercolano B., Bonnell I. A., 2012, MNRAS, 424, 377
Dale J. E., Ngoumou J., Ercolano B., Bonnell I. A., 2014, MNRAS, 442, 694
Deharveng L., Peña M., Caplan J., Costero R., 2000, MNRAS, 311, 329
Draine B. T., 2011, ApJ, 732, 100
Draine B. T., Lee H. M., 1984, ApJ, 285, 89
Draine B. T. et al., 2007, ApJ, 663, 866
Ercolano B., Gritschneder M., 2011, MNRAS, 413, 401
Fall S. M., Krumholz M. R., Matzner C. D., 2010, ApJ, 710, L142
Federrath C., Banerjee R., Clark P. C., Klessen R. S., 2010, ApJ, 713, 269
Ferland G. J., Korista K. T., Verner D. A., Ferguson J. W., Kingdon J. B., Verner E. M., 1998, PASP, 110, 761
Fukushima H., Yajima H., Sugimura K., Hosokawa T., Omukai K., Matsumoto T., 2020, MNRAS, 497, 3830
Gavagnin E., Bleuler A., Rosdahl J., Teyssier R., 2017, MNRAS, 472, 4155
Geen S., Hennebelle P., Tremblin P., Rosdahl J., 2015, MNRAS, 454, 4484
Geen S., Soler J. D., Hennebelle P., 2017, MNRAS, 471, 4844
Geen S., Watson S. K., Rosdahl J., Bieri R., Klessen R. S., Hennebelle P., 2018, MNRAS, 481, 2548
Harries T. J., 2015, MNRAS, 448, 3156
Harries T. J., Douglas T. A., Ali A., 2017, MNRAS, 471, 4111
Harries T. J., Haworth T. J., Acreman D., Ali A., Douglas T., 2019, Astron. Comput., 27, 63
Harris C. R. et al., 2020, Nature, 585, 357
Haworth T. J., Harries T. J., 2012, MNRAS, 420, 562
Haworth T. J., Harries T. J., Acreman D. M., Bisbas T. G., 2015, MNRAS, 453, 2277
Hollenbach D., McKee C. F., 1979, ApJS, 41, 555
Howard C. S., Pudritz R. E., Harris W. E., 2014, MNRAS, 438, 1305
Howard C. S., Pudritz R. E., Harris W. E., 2016, MNRAS, 461, 2953
Howard C. S., Pudritz R. E., Harris W. E., 2017, MNRAS, 470, 3346
Howard C. S., Pudritz R. E., Harris W. E., 2018, Nat. Astron., 2, 725
Hunter J. D., 2007, Comput. Sci. Eng., 9, 90
Ishiki S., Okamoto T., Inoue A. K., 2018, MNRAS, 474, 1935
Jones A. P., 2004, in Witt A. N., Clayton G. C., Draine B. T., eds, ASP Conf. Ser. Vol. 309, Astrophysics of Dust. Astron. Soc. Pac., San Francisco, p. 347
Kim J.-G., Kim W.-T., Ostriker E. C., 2018, ApJ, 859, 68
Krumholz M. R., Klein R. I., McKee C. F., 2007, ApJ, 656, 959
Krumholz M. R., Klein R. I., McKee C. F., Offner S. S. R., Cunningham A. J., 2009, Science, 323, 754
Kuiper R., Klahr H., Dullemond C., Kley W., Henning T., 2010, A&A, 511, A81

Kurucz R., 1993, ATLAS9 Stellar Atmosphere Programs and 2 km/s Grid. Kurucz CD-ROM No. 13. Smithsonian Astrophysical Observatory, Cambridge, MA, p. 13
Lada C. J., Lada E. A., 2003, ARA&A, 41, 57
Lanz T., Hubeny I., 2003, ApJS, 146, 417
Liow K. Y., Dobbs C. L., 2020, MNRAS, 499, 1099
Lopez L. A., Krumholz M. R., Bolatto A. D., Prochaska J. X., Ramirez-Ruiz E., 2011, ApJ, 731, 91
Lopez L. A., Krumholz M. R., Bolatto A. D., Prochaska J. X., Ramirez-Ruiz E., Castro D., 2014, ApJ, 795, 121
Lucy L. B., 1999, A&A, 344, 282
McKinney W., 2010, in van der Walt S., Millman J., eds, Proceedings of the 9th Python in Science Conference. p. 56
McLeod A. F., Dale J. E., Evans C. J., Ginsburg A., Kruijssen J. M. D., Pellegrini E. W., Ramsay S. K., Testi L., 2019, MNRAS, 486, 5263
Mathews W. G., 1967, ApJ, 147, 965
Mathis J. S., Rumpl W., Nordsieck K. H., 1977, ApJ, 217, 425
Matzner C. D., 2002, ApJ, 566, 302
Mellema G., Raga A. C., Canto J., Lundqvist P., Balick B., Steffen W., Noriega-Crespo A., 1998, A&A, 331, 335
Mellema G., Arthur S. J., Henney W. J., Iliev I. T., Shapiro P. R., 2006, ApJ, 647, 397
Mignon-Risse R., González M., Commerçon B., Rosdahl J., 2020, A&A, 635, A42
Offner S. S. R., Klein R. I., McKee C. F., Krumholz M. R., 2009, ApJ, 703, 131
Olivier G. M., Lopez L. A., Rosen A. L., Nayak O., Rieter M., Krumholz M. R., Bolatto A. D., 2020, preprint (arXiv:2009.10079)
Oort J. H., Spitzer Jr. L., 1955, ApJ, 121, 6
Osterbrock D., Ferland G., 2006, Astrophysics of Gaseous Nebulae and Active Galactic Nuclei, 2nd edn. University Science Books, Sausalito, CA
Pellegrini E. W., Baldwin J. A., Ferland G. J., 2011, ApJ, 738, 34
Peters T., Banerjee R., Klessen R. S., Mac Low M.-M., Galván-Madrid R., Keto E. R., 2010, ApJ, 711, 1017
Portegies Zwart S. F., McMillan S. L. W., Gieles M., 2010, ARA&A, 48, 431
Raga A. C., Cantó J., Rodríguez L. F., 2012, MNRAS, 419, L39
Rey-Raposo R., Dobbs C., Agertz O., Alig C., 2017, MNRAS, 464, 3536
Roman-Duval J., Jackson J. M., Heyer M., Rathborne J., Simon R., 2010, ApJ, 723, 492
Rosen A. L., Li P. S., Zhang Q., Burkhart B., 2019, ApJ, 887, 108
Russell S. C., Dopita M. A., 1992, ApJ, 384, 508
Sartorio N. S., Vandenbroucke B., Falceta-Goncalves D., Wood K., 2021, MNRAS, 500, 1833
Skinner M. A., Ostriker E. C., 2015, ApJ, 809, 187
Spitzer L., 1978, Physical Processes in the Interstellar Medium. Wiley-Interscience, New York
Tsang B. T.-H., Milosavljević M., 2018, MNRAS, 478, 4142
Vandenbroucke B., Wood K., 2019, MNRAS, 488, 1977
Walch S. K., Whitworth A. P., Bisbas T., Wünsch R., Hubber D., 2012, MNRAS, 427, 625
Zamora-Avilés M. et al., 2019, MNRAS, 487, 2200

This paper has been typeset from a TEX/LATEX file prepared by the author.